

<https://doi.org/10.1038/s44335-025-00042-4>

# Artificial synapse with tunable dynamic range for neuromorphic computing with ion intercalated bilayer graphene

Check for updates

Yuzhi He<sup>1</sup>, Purun (Simon) Cao<sup>2</sup>, Shahin Hashemkhani<sup>1</sup>, Yihan Liu<sup>1</sup>, Daniel Vaz<sup>1</sup>, Keya Joy<sup>2</sup>, Nathan Youngblood<sup>1</sup>, Rajkumar Kubendran<sup>1</sup>, M. P. Anantram<sup>2</sup> & Feng Xiong<sup>1</sup>

In neuromorphic computing, a tunable dynamic range in artificial synapses is crucial, as it allows devices to emulate the human brain's efficiency in processing complex information with analog programmable states. Here, we introduce an electrochemical random-access memory (ECRAM) based on bilayer graphene. Our device achieves a large and programmable dynamic range through lithium-ion ( $\text{Li}^+$ ) intercalation, pulse modulation, and geometric engineering. We systematically investigated how pulse parameters, including amplitude, duty cycle, frequency, and signal type, affect conductance and dynamic range. Our results demonstrate that higher pulse amplitudes and/or longer duty cycles enhance  $\text{Li}^+$  intercalation efficiency; while lower frequency pulse trains facilitate ion intercalation, significantly influencing conductance and dynamic range. Specifically, the dynamic range expanded by approximately 131% when increasing the pulse amplitude from  $\pm 0.1 \text{ V}$  to  $\pm 0.3 \text{ V}$ , and by about 1011% when adjusting the duty cycle from 10% to 90%. Additionally, we explored how geometric factors such as channel length in bilayer and multi-layer graphene and the introduction of hole structures may affect intercalation kinetics and subsequently device performance. First-principles density functional theory (DFT) calculations were also performed to support that the interlayer space in bilayer graphene is energetically favorable for Li transport, and that hole structures promote efficient Li intercalation by providing barrierless pathways through the exposed edges of the bilayer. These findings confirm bilayer graphene as a promising material for developing high-performance artificial synapses with tunable characteristics.

The rapid development of artificial intelligence and machine learning increasingly highlights the limitations of traditional computing architectures<sup>1,2</sup>. Traditional digital computing systems suffer from the von Neumann bottleneck, where the separation of processors and memory leads to frequent data transmission, consuming significant energy and restricting high-performance computing development<sup>3–7</sup>. Inspired by the remarkable efficiency of the human brain in performing specialized tasks, neuromorphic computing has emerged as a promising approach to overcome these challenges, with artificial synapses as fundamental elements<sup>8–11</sup>. These artificial synapses exhibit dynamic behavior similar to biological synapses, enabling real-time learning and memory functions.

One crucial characteristic of artificial synapses is dynamic range (DR), defined as the ratio of the change in conductance to the minimum conductance  $DR = \frac{G_{\text{Max}} - G_{\text{Min}}}{G_{\text{Min}}} = \frac{\Delta G}{G_{\text{Min}}}$ . Note that this definition differs from the

conventional form  $\frac{G_{\text{Max}}}{G_{\text{Min}}}$  by subtracting one, emphasizing relative conductance modulation beyond the baseline<sup>12</sup>. This relative-change-based definition provides clearer interpretability in practical neuromorphic scenarios, such as neural network training and STDP updates, where performance is often measured by the extent of synaptic weight updates rather than absolute limits alone<sup>13,14</sup>. A tunable dynamic range enhances adaptability, optimizing power consumption and computational accuracy according to specific task requirements, such as low-precision inference or high-precision training. Adjustable dynamic range improves weight update processes, reduces nonlinear errors, and enhances computational stability<sup>5,15</sup>. For instance, in biohybrid systems, artificial synapses must process sensory inputs of varying intensities to facilitate real-time adaptive responses in soft robotics and prosthetic devices, relying on a broad dynamic range to convert both weak and strong signals into graded outputs<sup>16</sup>.

<sup>1</sup>Department of Electrical and Computer Engineering (ECE), University of Pittsburgh, Pittsburgh, PA, 15213, USA. <sup>2</sup>Department of Electrical and Computer Engineering (ECE), University of Washington, Seattle, WA, 98195, USA. e-mail: [f.xiong@pitt.edu](mailto:f.xiong@pitt.edu)

Additionally, tunable dynamic range allows neuromorphic devices to handle input signals with diverse intensities. This flexibility enables smaller, more precise pulses for adjusting synaptic weights, lowering operational energy consumption. For example, Tang et al. demonstrated switching energies as low as approximately 1 fJ per update by leveraging a wide dynamic range<sup>17</sup>.

However, achieving tunable dynamic range in artificial synapses remains challenging due to limitations in traditional materials and devices. Tunable dynamic range is particularly important because different neuromorphic tasks require different levels of conductance modulation. In many cases, operating within a limited and task-optimized dynamic range can significantly reduce energy consumption by avoiding excessive ion migration or charge transfer. Tunability can be achieved either by dynamically adjusting a single device's response through pulse parameters or by fabricating synapses with tailored ranges for specific computational functions. Achieving this control requires material systems and device architectures that enable stable, reversible, and energy-efficient conductance modulation. Memristors, widely studied, often exhibit asymmetric and nonlinear conductance switching, leading to unpredictable modulation<sup>4</sup>. In contrast, electrochemical random-access memory (ECRAM) achieves nearly linear weight updates and extremely low-energy switching through ion intercalation reactions, showcasing its potential in high-speed, low-power neuromorphic systems<sup>9,17–20</sup>. In ECRAM devices, ions such as lithium or hydrogen are inserted into or extracted from active materials—typically metal oxides (e.g.,  $\text{WO}_3$ ) or two-dimensional materials—using tailored electrical pulses. Talin et al. introduced various ECRAM structures, including devices based on  $\text{Li}^+$  or  $\text{H}^+$  insertion into transition metal oxides, such as Li-ion synaptic transistors (LISTA) using a  $\text{LiCoO}_2/\text{LiPON}/\text{Si}$  stack, achieving linear conductance modulation and ultralow switching energies<sup>21</sup>. Additionally, devices using oxygen vacancy modulation in metal oxides, such as  $\text{WO}_3$ -based ECRAM with solid electrolytes like yttria-stabilized zirconia (YSZ) or gadolinium-doped ceria (GDC), achieve analog switching via reversible vacancy concentration tuning<sup>22</sup>. ECRAM devices based on organic or coordination polymers and two-dimensional materials exploit their large interfacial areas and adjustable electronic properties for dynamic, reversible conductance control<sup>23</sup>.

In recent years, ECRAM has gained significant attention as a leading candidate for neuromorphic synaptic devices, owing to its low-energy operation, high linearity, and analog programmability through electrochemical ion migration. A comprehensive review by Kwak et al. emphasized that ECRAM, particularly those using  $\text{Li}^+$ ,  $\text{H}^+$ , or  $\text{O}^{2-}$  ions, can achieve over 1000 distinct conductance states with symmetric updates, making them well-suited for analog matrix operations in in-memory computing<sup>9</sup>. Moreover, Mukhtar et al. further detailed that Li-ion-based ECRAMs, especially those using layered materials like  $\text{Li}_{1-x}\text{CoO}_2$  or  $\alpha\text{-MoO}_3$ , offer fast ion diffusion, low activation energy, and high endurance, enabling precise control over dynamic range while minimizing energy consumption<sup>24</sup>. This capacity for gradual and stable conductance tuning via ion intercalation aligns closely with neuromorphic computing demands, such as real-time learning and spike-timing-dependent plasticity (STDP). In parallel, graphene-based synaptic devices have shown promise due to their excellent carrier mobility and electrochemical stability. Notably, monolayer graphene transistors gated with hydrogen ion electrolytes have manipulated the electric conductivity of graphene transistors, resulting in a high on/off resistance ratio, a well-defined set/reset voltage, and a prolonged retention time<sup>25</sup>. Additionally, a graphene synaptic transistor with an ion-gel gated long-channel structure has been shown to mimic key synaptic behaviors—including paired-pulse facilitation, long-term potentiation, and learning functions—while also enabling environmental sensing such as humidity perception, thus integrating memory, computation, and sensing in a single neuromorphic platform<sup>26</sup>.

Among candidates for artificial synaptic devices, bilayer graphene ECRAM stands out due to its unique electronic properties, including high carrier mobility and highly tunable carrier density through electrochemical intercalation and de-intercalation<sup>27–39</sup>. These characteristics enable dynamic

tuning of bilayer graphene ECRAM's dynamic range through intercalation<sup>40–43</sup>. This approach effectively addresses traditional material limitations and enhances synaptic control, improving neuromorphic system adaptability and efficiency. Understanding how different intercalation conditions and device configurations influence bilayer graphene ECRAM's dynamic range is critical for developing high-performance tunable artificial synapses<sup>44</sup>. While initial studies show that intercalation can effectively alter bilayer graphene's carrier density and resistance states, the combination of geometric engineering (e.g., channel length, hole patterns) with controlled  $\text{Li}^+$  intercalation remains underexplored. Such an approach could enable systematic tuning of dynamic range, enhancing device adaptability for task-specific neuromorphic performance. In this context, our work explores how coupling geometric design with ion intercalation strategies can unlock new avenues for enhancing bilayer graphene ECRAM performance, addressing key challenges in dynamic range tuning and energy-efficient synaptic behavior.

In this work, we demonstrate a bilayer graphene ECRAM with a tunable dynamic range achieved via  $\text{Li}^+$  intercalation and electrical pulse modulation. By varying electrical input configurations, we show that the maximum and minimum  $\text{Li}^+$  intercalation stages significantly correlate with pulse amplitude, duty cycle, and frequency, while waveform shape has a limited impact. Specifically, our results reveal substantial expansion of  $\text{Li}^+$  intercalation stages with increased pulse amplitude and duty cycle, and a notable reduction in intercalation range with increasing frequency. Furthermore, we examined geometric factors, including graphene flake length and thickness, and performed comparative analyses between devices with etched channel holes and pristine counterparts. Results demonstrate that incorporating holes markedly enhances dynamic performance. Our study provides valuable insights for optimizing bilayer graphene ECRAM design by systematically evaluating geometric factors and input signal parameters, contributing to high dynamic performance.

## Results

### Device fabrication and characterization

A schematic illustration of a biological synapse and our device fabrication process is shown in Fig. 1a, b. Metal Au/Pt gates were patterned adjacent to the exfoliated bilayer graphene. Subsequently, a solution of  $\text{LiFePO}_4$  (lithium-ion phosphate, LFP) was applied onto the gates and dried. Afterward, a solid electrolyte consisting of  $\text{LiClO}_4$  in poly(ethylene oxide) (PEO) was introduced and cured, enabling ionic exchange between the graphene and LFP<sup>45,46</sup>. An optical micrograph of the bilayer graphene ECRAM device is presented in Fig. 1c. The dark region at the top corresponds to the LFP layer, which covers the underlying ionic gates. The bilayer graphene flake and metal contacts appear near the center, with a white dashed circle indicating the portion of the device shown at higher magnification in the inset. The inset clearly displays the bilayer graphene channel bridging the gold electrodes, highlighting the detailed geometry of the contacts and the flake. The scale bars in the main image and inset are 200  $\mu\text{m}$  and 20  $\mu\text{m}$ , respectively. To confirm the bilayer nature of graphene, Raman spectroscopy and atomic force microscopy (AFM) were performed, as shown in Fig. 1d, e, and S1. The Raman spectrum demonstrates nearly equal intensities of the G and 2D peaks, confirming the presence of bilayer graphene<sup>47</sup>. The AFM image indicates a graphene thickness of 0.718 nm, closely matching previously reported values for bilayer graphene<sup>48</sup>.

### Electrochemical lithium intercalation

The static intercalation and de-intercalation processes between the bilayer graphene channel and two gates are studied, as illustrated in Fig. 2. Figure 2a shows a schematic of the reversible electrochemical lithium-ion intercalation process in bilayer graphene<sup>49,50</sup>. A small current was applied through an external circuit from graphene to LFP to initiate intercalation. During this process,  $\text{Li}^+$  primarily enter between the graphene layers<sup>40</sup>. The lithium component in graphene increases carrier density and electrical conductivity<sup>41</sup>. Bilayer graphene offers sufficient interlayer sites for intercalation while maintaining an adequately thin structure.

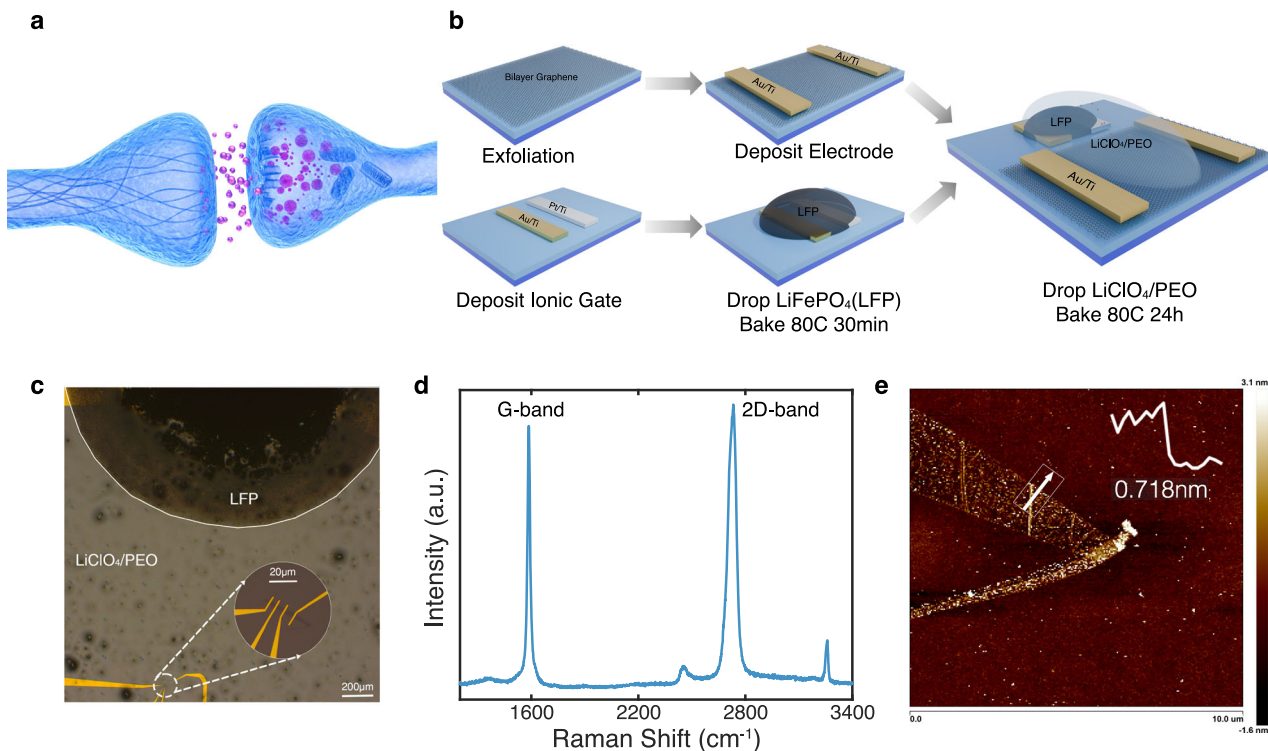


**Fig. 1 | Bilayer graphene ECRAM.** **a**, Schematic of a biological synapse. (©Alex Mit/Adobe Stock). **b**, Schematic of the fabrication process for bilayer graphene ECRAM and dual ion gate Au/LFP and Pt/LFP. **c**, Optical image of the device. The upper dark region is LFP with the ionic gates positioned under it. The white dashed circle shows

the right inset, which is an enlarged image of the graphene channel. **d**, Raman spectrum measured on the graphene channel. **e**, AFM measurement of the graphene flake.

Figure 2b illustrates that the potential of the bilayer graphene electrode gradually decreases from the initial 0 V to about −1.8 V. An apparent plateau appears between 200s and 2200s, where the potential decreases slowly. Subsequently, the potential decreases rapidly around 4500s and eventually stabilizes between −1.6 V and −1.8 V. This plateau corresponds to the gradual lithium-ion intercalation transitioning from the C state to C<sub>6</sub>LiC<sub>6</sub>, indicating controlled intercalation kinetics<sup>40,51–53</sup>. Conversely, the Pt ion gate system exhibits different kinetic characteristics: the potential rapidly decreases from about −0.4 V to −1.6 V at approximately 1000s, then enters a relatively stable declining phase, finally stabilizing around −1.9 V. This rapid decline indicates Pt's strong catalytic activity accelerates lithium-ion reduction and intercalation, significantly enhancing interface reaction rates. However, excessively rapid processes may lead to side reactions or interface inhomogeneity, adversely impacting the device's long-term cycling stability.

Additionally, considering LFP's stable open-circuit voltage (OCV), both Au and Pt systems stabilize between −1.6 V and −1.9 V. This demonstrates that intercalation increases the lithium content in graphene, causing the graphene electrode potential to gradually decrease and stabilize<sup>54</sup>. Based on this analysis, we selected Au as the ion gate for subsequent experiments. Au's main advantages include: first, low catalytic activity and high chemical inertness, allowing slower and more uniform lithium-ion intercalation, ensuring a stable and controllable transformation from C to C<sub>6</sub>LiC<sub>6</sub>; second, a clearly defined plateau phase beneficial for quantitative analysis of intercalation dynamics and diffusion parameters extraction; third, once the Au system reaches a stable state around −1.8 V, it exhibits high repeatability and stability, facilitating the comparison and analysis of subsequent electrochemical test data. In contrast, Pt's strong catalytic activity accelerates intercalation but can lead to rapid potential drops, less uniform ion distribution, and possible side reactions, compromising device stability and reproducibility. Therefore, Au was chosen as the gate material to ensure consistent and analyzable device responses in all subsequent experiments.

Given these considerations, we selected 1.8 V as the baseline potential for subsequent pulse tests. A pulse amplitude of ±0.2 V was designed to introduce perturbations under near-equilibrium conditions, facilitating the exploration of lithium-ion intercalation and de-intercalation dynamics in bilayer graphene. Additionally, this pulse scheme induces dynamic responses within the system, maintaining operation in a stable lithiated state. This enables precise control and in-depth analysis of the electrochemical reaction mechanisms.

To complement the experimental investigation of Li intercalation, we carried out density functional theory (DFT) calculations to evaluate the energetic landscape for intercalation of Li in pristine AB-stacked bilayer graphene. After structural relaxation, we compared the total energies of three configurations: Li intercalated between the two graphene layers, adsorbed on top of the bilayer surface, and far from the bilayer in vacuum. Taking the interlayer position as the reference (0 eV), the surface-adsorbed Li is found to be 0.682 eV higher in energy, and the vacuum-separated Li is 1.874 eV higher. As shown in Fig. 2c, these results indicate that Li is most stable when located in-between the bilayers, confirming that the bilayer structure favors interlayer intercalation over surface adsorption or remaining outside the system.

In addition to total energy comparisons of stable configurations, we also calculated the energy barrier of Li diffusion within the interlayer space using the climbing-image nudged elastic band (CI-NEB) method. As shown in Fig. 2d, the calculated diffusion barrier for Li migration between adjacent intercalation sites was found to be only 0.07 eV, suggesting that Li can migrate freely once intercalated. Similar low diffusion energy barriers have been reported in previous studies<sup>55</sup>. These computational findings further reinforce the notion that the interlayer region is energetically favorable for Li intercalation and transport.

**Effect of pulse modulation on conductivity and dynamic range**  
Pulse modulation parameters play a crucial role in device conductivity and dynamic range. We systematically studied different pulse amplitudes, duty

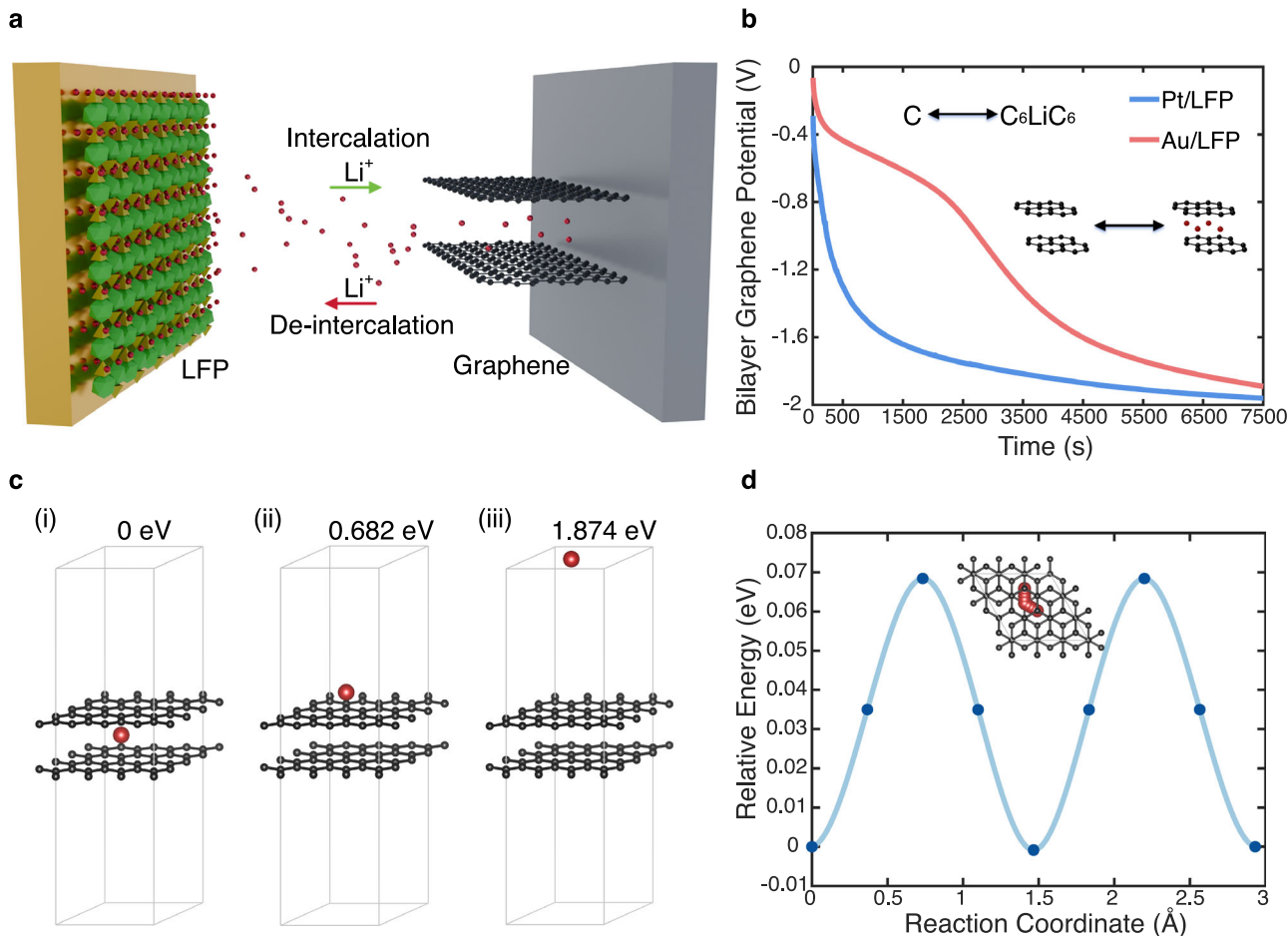


**Fig. 2 | Lithium-ion intercalation dynamics in bilayer graphene.** **a**, Schematic of the reversible electrochemical lithium intercalation process. The double arrows indicate the intercalation and de-intercalation process, where electrons and lithium ions flow into and out of the graphene working electrode. **b**, Time-dependent potential of the bilayer graphene electrode during lithium-ion intercalation under galvanostatic conditions with Pt/LFP and Au/LFP gate configurations. **c**, Total energy comparison of a Li atom placed in three distinct configurations: (i) intercalated between the graphene layers (reference, 0 eV), (ii) adsorbed on the outer

surface of the top graphene layer (0.682 eV higher), and (iii) positioned far above the bilayer in vacuum (1.874 eV higher). These results indicate a strong thermodynamic preference for Li to occupy the interlayer space. **d**, CI-NEB calculations showing energy barrier and diffusion path of Li migrating between adjacent intercalation sites within the interlayer region. The energy barrier is low, approximately 0.07 eV, indicating favorable in-plane diffusion once Li is intercalated. The inset illustrates the atomic trajectory along the diffusion pathway.

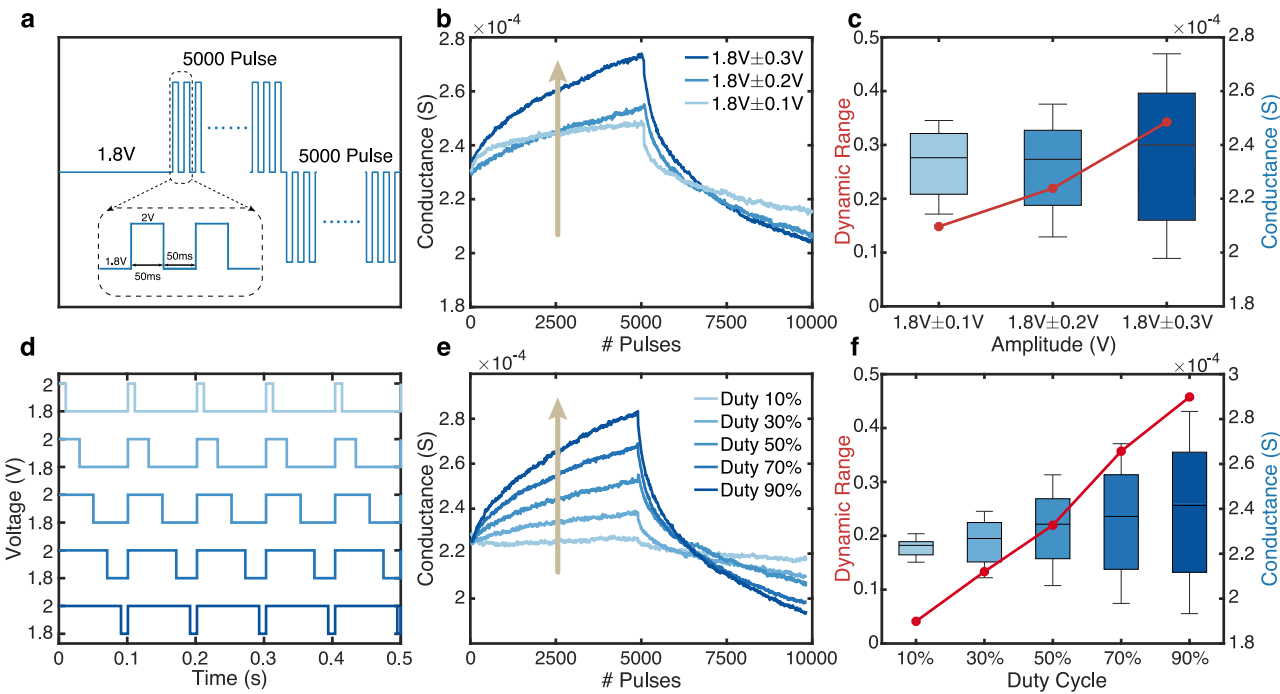
cycles, and frequencies to understand their effects on lithium-ion intercalation, finding that these parameters directly impact graphene device performance. Figure 3 illustrates how varying pulse settings affect conductivity and dynamic range in bilayer graphene ECRAM. Initially, we applied a series of positive pulses followed by negative pulses, as shown in Fig. 3a. A DC voltage of 1.8 V stabilizes lithium-ion intercalation based on the plateau observed in Fig. 2b. Subsequently, 5000 positive square pulses (pulse width 0.05 s, duty cycle 50%) were applied for intercalation, achieving maximum conductance ( $G_{\max}$ ). Then, 5000 negative pulses were applied for de-intercalation, reaching minimum conductance ( $G_{\min}$ ). To ensure controlled and repeatable conductance modulation, we chose 5000 pulses in each direction to clearly illustrate the transition between  $G_{\max}$  and  $G_{\min}$ . These values are not intrinsic physical limits of the material but are operational boundaries defined under specific pulse conditions. Since  $G_{\max}$  and  $G_{\min}$  in continuously tunable devices depend on the applied pulse amplitude, frequency, and duty cycle, we define them here as the maximum and minimum conductance values achieved under standardized, repeatable conditions. This definition enables consistent comparison across different experiments and allows adjustment of the dynamic range to suit specific application requirements.

Figure 3b shows conductance changes under  $\pm 0.1$  V,  $\pm 0.2$  V, and  $\pm 0.3$  V pulses, while Fig. 3c presents the corresponding dynamic range (blue line) and

conductance distribution (red box chart). Higher-amplitude pulses increase the internal electric field, enhancing the driving force for  $\text{Li}^+$  migration. The stronger electric field enables  $\text{Li}^+$  to overcome diffusion barriers and local potential wells more effectively, increasing ion intercalation into bilayer graphene. From an intercalation viewpoint, elevated electric fields modify local energy surfaces, improving  $\text{Li}^+$  diffusion. The increased carrier concentration results in higher conductance and an expanded dynamic range.

Further analysis explored varying duty cycles (10%–90%) at fixed amplitude ( $\pm 0.2$  V) and frequency (10 Hz). Figure 3e demonstrates that higher duty cycles produce greater conductance over time, with Fig. 3f showing an upward trend in dynamic range. A longer “on” period per cycle allows  $\text{Li}^+$  sufficient time to overcome energy barriers and complete intercalation, enhancing overall efficiency. Extended high-voltage periods also maintain ion distribution within graphene, minimizing reverse diffusion or partial intercalation that might occur with shorter pulses. Quantitatively, the DR increased by ~131% (from 0.1483 to 0.3425) when the pulse amplitude was raised from  $\pm 0.1$  V to  $\pm 0.3$  V, and by ~1011% (from 0.0412 to 0.4577) as the duty cycle increased from 10% to 90%, as shown in Fig. 3c, f.

Additional experiments analyzed pulse frequency (2–20 Hz), maintaining a 50% duty cycle and  $\pm 0.2$  V amplitude. In Fig. S2b, device conductance decreases as frequency increases, at 2 Hz the DR was 0.4782, while at 20 Hz it dropped to 0.1597, a 67% decrease, indicating that high-



**Fig. 3 | Effect of input pulse's modulation on graphene ECRAM's dynamic range.** Schematic of the pulse sequence of **a** DC, 5000 positive pulses, 5000 negative pulses. Bilayer graphene ECRAM's conductance changes when input pulses are **b** positive and negative pulse trains of different amplitudes; **e** pulses of different duty cycles.

Bilayer graphene ECRAM's dynamic range when input pulses are **c** positive and negative pulse train of different amplitudes; **f** pulses of different duty cycles, ranging from 10% to 90%.

frequency pulses provide insufficient time for full  $\text{Li}^+$  intercalation. From a lithium-ion intercalation perspective, ion movement is thermally activated; shorter pulses at higher frequencies limit ion migration across potential barriers. Figure S2c shows the resulting dynamic range and conductance distribution. Higher frequencies reduce dynamic range because shorter pulses weaken intercalation effects and cumulative conductivity gains.  $\text{Li}^+$  lacks sufficient time to integrate into graphene lattices, leading to less effective intercalation at high frequencies.

A comparative evaluation of square, ramp, and sinusoidal pulse waveforms was conducted at identical amplitude and frequency. Figure S2e illustrates minimal conductance differences among waveforms, as total energy and high-voltage duration remain similar. This minimal variation can be attributed to the similar total energy delivered and comparable high-voltage durations across different waveforms. Since  $\text{Li}^+$  intercalation is a thermally activated process, slight variations in voltage shape do not significantly affect the kinetics, provided that the energy and time windows are preserved. Thus, the device performance remains robust against waveform variations, enhancing its operational reliability and simplifying circuit design.

To clarify the combined effects of frequency, duty cycle, and amplitude, we selected two groups of three distinct pulse conditions (low frequency/high amplitude, moderate frequency/moderate amplitude, high frequency/low amplitude) achieving identical dynamic ranges, as shown in Fig. S2f. Within the same measurement period, conductance changes appear similar once a stable  $\text{Li}^+$  distribution is reached. However, the time required to achieve specific conductance levels differs significantly across conditions, demonstrating how certain parameter combinations accelerate or delay intercalation onset. Although the final dynamic range converges, the pathway and speed to that state vary significantly. This highlights the importance of aligning pulse parameters with inherent intercalation kinetics for efficient neuromorphic or ECRAM applications.

### Geometric effects on device performance

The geometric structure of the graphene channel is another crucial factor influencing the intercalation process and ECRAM's dynamic performance, as ions intercalate through graphene's lateral edges. We then investigated

the impact of channel length and layer number on the ECRAM's dynamic range<sup>56</sup>. To avoid the influence of contact resistance on our dynamic range calculations, we employed a four-terminal measurement method for conductance evaluation<sup>57</sup>. Specifically, two external electrodes supply current to the device, while two internal electrodes measure accurate conductivity through voltage scanning, as illustrated in Fig. 4a.

Figure 4b shows how the dynamic range of bilayer graphene devices (Fig. S3) changes over time under lithium-ion intercalation pulses. The intercalation pulses for the bilayer samples were square pulses with an amplitude of 0.2 V and a reference voltage of 1.8 V (frequency 10 Hz, duty cycle 50%). Conductance measurements were taken every 250 s. Since bilayer graphene contains only one interlayer, measurements continued for 1250 s until the device approached saturation. The results show that the dynamic range increases with device length, suggesting that longer graphene paths accommodate more  $\text{Li}^+$ , leading to enhanced intercalation and a broader conductivity range.

To verify the generality of this phenomenon, we also prepared multi-layer graphene ECRAM devices with comparable dimensions, shown in Fig. S4, and characterized them using Raman spectroscopy and AFM (Figs. S5 and S6)<sup>58</sup>. For these devices, we referenced previous galvanostatic charge-discharge (GCD) measurements, which indicated that multi-layer graphene-LFP systems stabilize at approximately 2.7 V<sup>50</sup>. Thus, we selected 2.7 V as the baseline voltage and +0.5 V as the intercalation pulse amplitude (frequency 10 Hz, duty cycle 50%), conducting conductance measurements every 1000 s. As depicted in Fig. 4c and S7, multi-layer graphene provides additional  $\text{Li}^+$  intercalation sites and interlayer diffusion pathways, allowing ions to intercalate across multiple planes. This significantly enhances overall conductivity. Multi-layer devices demonstrate higher dynamic ranges due to their complex structures. Both bilayer and multi-layer graphene devices show increased dynamic range with channel length, indicating a common underlying mechanism for  $\text{Li}^+$  intercalation. Because bilayer graphene is structurally simpler, it enables easier modeling and detailed analysis of intercalation processes. Consequently, our primary experimental focus remains on bilayer graphene, while multi-layer experiments confirm the general applicability of our findings.

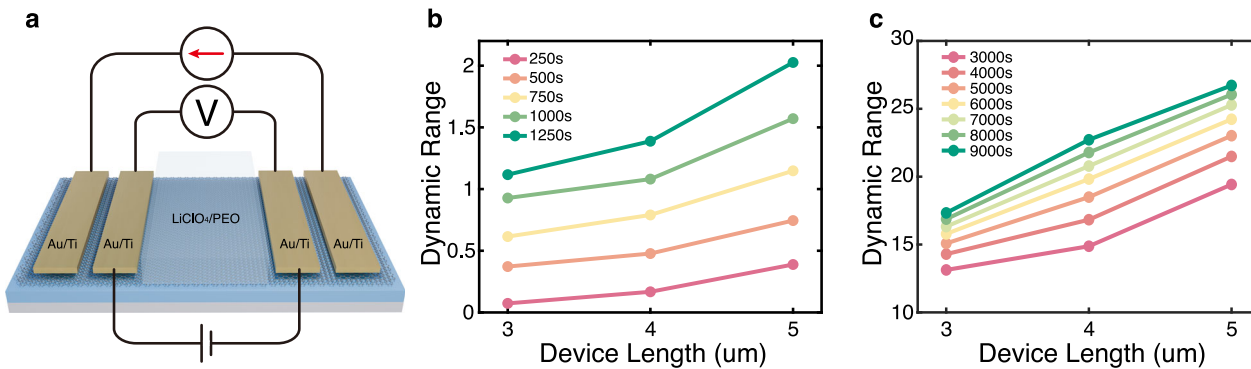


**Fig. 4 | Effect of geometric structure on graphene ECRAM's dynamic range.** **a** 4 terminal measurement setup. Dependence of dynamic range on channel length of **b** bilayer sample and **c** multi-layer sample.

To further investigate possible lithium-ion intercalation pathways in bilayer graphene in an effort to accelerate Li intercalation and improve dynamic performance, we began by exploring the process computationally using density functional theory (DFT). Specifically, we compared two representative routes: insertion through a point defect (a single-carbon vacancy in the top graphene layer) versus insertion from the edge of the bilayer, which mimics experimentally engineered hole structures.

To explore defect-assisted top insertion, we computed the minimum energy path for Li to enter through a single-carbon (1 C) vacancy using the climbing-image nudged elastic band (CI-NEB) method. In bilayer graphene with a 1 C vacancy in the top layer, the insertion barrier was found to be high—approximately 2.7 eV (Fig. 5a). These large barriers demonstrate that, even in the presence of atomic-scale defects, Li penetration through a vacancy site is suppressed, making this pathway unlikely to contribute meaningfully to Li intercalation under experimentally relevant conditions. The results suggest that while point defects locally disrupt the graphene lattice, they do not offer an efficient entry channel for Li.

In contrast, lithium intercalation from the edge of bilayer graphene proved to be significantly more favorable. To model this, we constructed hydrogen-terminated nanoribbon structures with both armchair and zigzag edge terminations, following established approaches used in prior studies<sup>59,60</sup>. We calculated the total energy of a Li atom placed at increasing distances from the edge (5 Å, 3 Å, 1 Å away), as well as the fully intercalated state. In both geometries, the intercalated position near the edge was the global energy minimum, while Li atoms farther outside the ribbon were energetically less favorable by up to ~1.8 eV (armchair) and ~2.4 eV (zig-zag), as shown in Fig. 5b, c. It is also notable that the zigzag edge provided a larger energy drop, which may suggest enhanced Li trapping and potentially more favorable intercalation behavior compared to armchair edges.

To assess the accessibility of edge insertion, we further performed CI-NEB calculations for Li transitioning from a site 5 Å outside the bilayer edge to the intercalated configuration. Remarkably, we observed no energy barrier along this path, indicating a completely barrierless insertion process from the edge, as shown in Fig. 5d, e. This finding stands in sharp contrast to the high barriers encountered for vacancy-mediated top insertion and, in combination with previous results, strongly suggests that edge sites, which are functionally equivalent to experimentally created hole structures, serve as the dominant channels for Li intercalation into bilayer graphene.

Building upon these findings, we attribute the increase in dynamic range to enhanced lithium-ion intercalation resulting from longer graphene channels. Extended channel lengths provide larger areas for Li<sup>+</sup> diffusion pathways, allowing more lithium ions to intercalate within a given time. This increases conductance modulation and thus expands the dynamic range. However, simply increasing channel length is not the only effective way to enhance lithium-ion intercalation. To accelerate Li<sup>+</sup> intercalation and improve dynamic performance without enlarging device size, we explored structural engineering methods to increase active edge length. Specifically, we introduced elongated holes into bilayer graphene channels (Fig. 6a),

creating additional entry points for lithium ions. Theoretically, Li<sup>+</sup> intercalates into bilayer graphene primarily through its edges<sup>40,61,62</sup>. Therefore, devices with increased holes effectively provide more entry channels (Fig. 6b) for Li<sup>+</sup>, improving intercalation rates and conductivity. We measured conductance using a four-terminal method, where outer electrodes supply a small constant current and inner electrodes measure voltage. As shown in Fig. 6c, both single-hole (SH) and double-hole (DH) devices achieve higher conductance than the pristine (P) device at the same intercalation duration. Compared to pristine devices (DR = 10.064), the double-hole (DH) devices achieved a DR of 21.94, reflecting a 118% enhancement. However, initially, DH does not outperform SH because the ion supply is limited by the ion concentration in the ionic liquid. In our current device configuration, the electrolyte is manually applied as a droplet, which limits how closely the ion gate can be positioned relative to the graphene channel. This introduces a spatial separation between the ion gate and the active region, increasing the diffusion distance for Li<sup>+</sup> ions and reducing the efficiency of ion delivery. As a result, during early stages of intercalation—particularly in devices with enhanced edge access such as double-hole structures—the ion supply capability of the electrolyte becomes the rate-limiting factor rather than the intercalation kinetics of the graphene itself. This limitation underscores the importance of optimizing both the ionic conductivity and the spatial distribution of the electrolyte. Future improvements could include the development of solid-state electrolytes with higher ionic mobility and controlled deposition methods, allowing uniform and conformal coverage with minimal separation from the active region. Such advances would reduce ion migration pathways, improve supply uniformity, and support faster, more efficient intercalation dynamics, ultimately enhancing device performance and scalability. Figure 6d presents a box plot of conductance measured over 3000 s. DH exhibits higher median conductance and a broader range, emphasizing its enhanced capacity for achieving extended dynamic range. From an application perspective, this hole-based approach effectively shortens the intercalation pathway and increases edge sites, enabling faster attainment of desired conductance and improved ECRAM performance.

## Discussion

In this study, we demonstrated that the dynamic range of bilayer graphene ECRAM devices can be effectively tuned by adjusting pulse parameters and optimizing geometric design. To support the experimental investigation of electrochemical Li<sup>+</sup> intercalation, which serves as the central mechanism enabling programmable conductance, we performed first-principles DFT calculations to examine the underlying energetics of Li behavior in bilayer graphene. These simulations confirm that the interlayer space provides a highly energetically favorable environment for Li intercalation, and reveal that once inserted, Li can diffuse relatively easily within the interlayer region with minimal energy barrier. Then, we experimentally demonstrate that the reversible lithium-ion intercalation into bilayer graphene is significantly influenced by the ion gate material. Gold is selected for its low catalytic activity and distinct voltage plateau, which enables controlled and stable

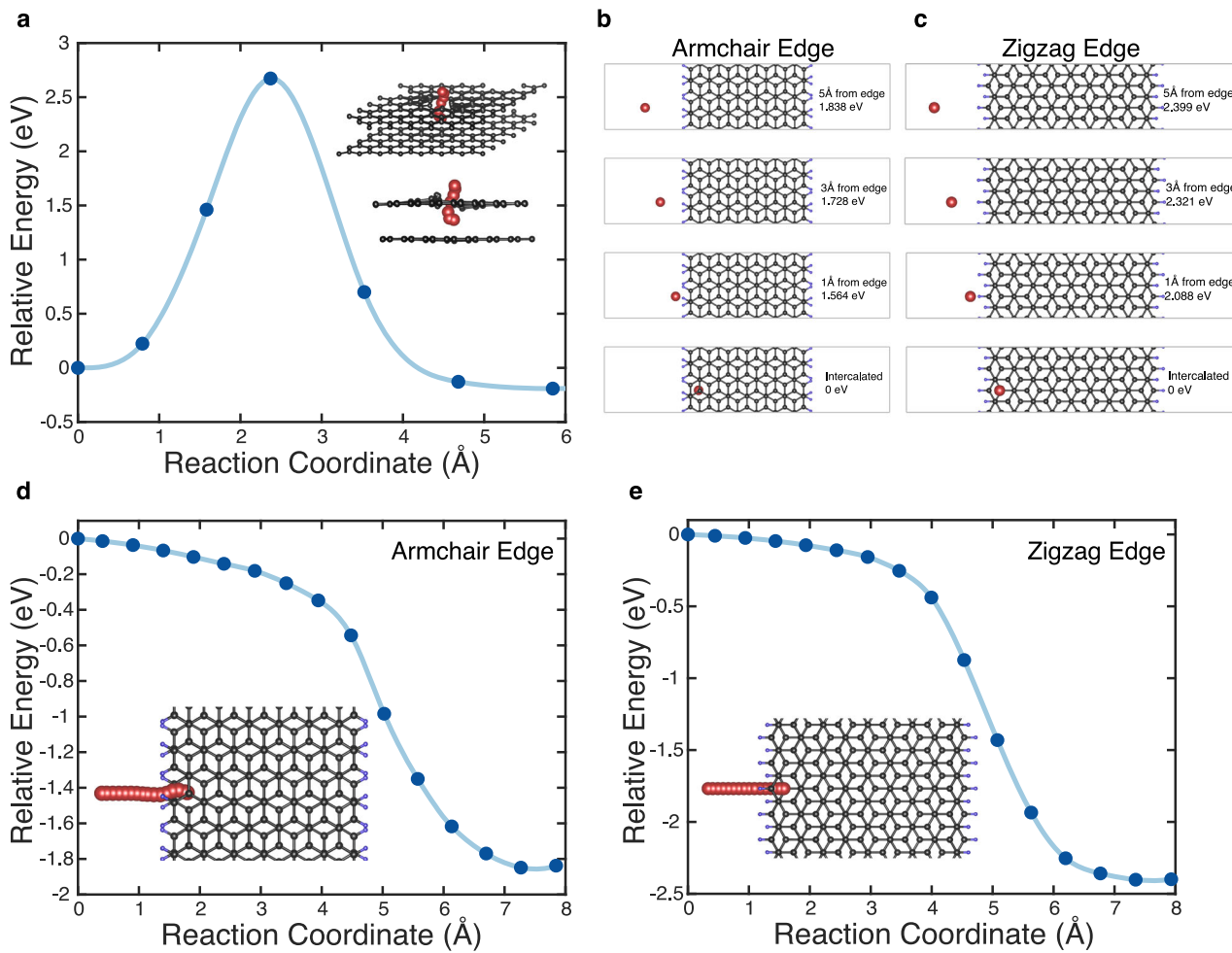


**Fig. 5 | Comparison between vacancy-assisted and edge-assisted Li insertion pathways in AB-stacked bilayer graphene.** aCI-NEB calculations showing energy barrier and insertion path of Li insertion through a single-carbon (1C) vacancy in the top graphene layer, showing a high energy barrier of approximately 2.7 eV. The inset illustrates the atomic trajectory along the insertion pathway. b, c Relative total energies of a Li atom placed at varying distances (5 Å, 3 Å, 1 Å) from hydrogen-terminated edges in nanoribbon models with armchair (b) and zigzag (c)

terminations. In both cases, the intercalated configuration is used as the reference (0 eV), and Li is increasingly stabilized as it approaches the edge. d, e CI-NEB calculations showing energy barrier and insertion path of Li from 5 Å outside the edge into the bilayer graphene structure for armchair (d) and zigzag (e) edges. The inset illustrates the atomic trajectory along the insertion pathway. Both cases show negligible energy barriers, indicating that edge-driven intercalation is favorable.

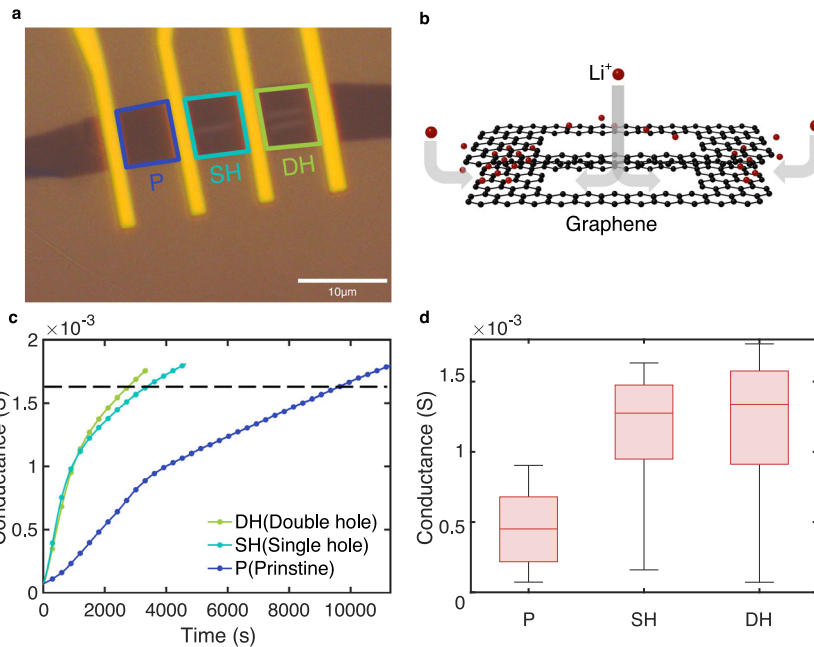
intercalation. Subsequent pulse tests conducted around this equilibrium potential effectively probe lithium-ion dynamics and facilitate detailed analysis of intercalation mechanisms. We observed that pulse parameters, such as amplitude and duty cycle, significantly impact the  $\text{Li}^+$  intercalation process. Higher pulse amplitude provides a stronger electric field driving force, while an extended duty cycle allows sufficient time for ions to overcome energy barriers and intercalate into the graphene layers, thus enhancing device conductance. Further analysis indicated that increased electric field strength optimizes ion distribution, aligning with previously reported pulse modulation strategies in literature<sup>17,63–66</sup>. For applications not requiring excessively large dynamic ranges, pulses with smaller amplitudes or shorter duty cycles can reduce  $\text{Li}^+$  intercalation, thus decreasing conductive gain and energy consumption. This strategy conserves power while satisfying lower dynamic range needs. Balancing dynamic range and power consumption during device design ensures overall performance meets expectations.

A key trade-off observed in our study is between switching speed and dynamic range. As shown in Fig. S2, higher pulse frequencies limit lithium-ion intercalation, resulting in reduced conductance modulation and dynamic range. This occurs because ion transport is thermally activated and

requires sufficient time during each pulse for effective intercalation. At high frequencies, shortened pulse durations restrict ion migration, limiting device response. While low-frequency operation maximizes dynamic range, neuromorphic systems may prioritize speed over range in certain tasks. Moderate frequencies combined with optimized pulse amplitude and duty cycle can still yield useful performance. For neuromorphic applications requiring fast response, pulse parameters must be carefully adjusted to maintain acceptable performance. This trade-off highlights the need for task-specific pulse optimization in future device integration.

Comparative analyses of various pulse waveforms indicated that total energy and effective “on” time are the primary factors, whereas slight variations in waveform shape minimally affect intercalation dynamics. Practically, ensuring adequate energy and time windows grants high device tolerance to pulse shape variations, simplifying circuit designs. Additional experimental data also showed that waveform differences mainly involve slight shifts in energy distribution without significantly affecting ion intercalation kinetics. Such flexibility in pulse shapes improves operational robustness, enhancing fault tolerance in neuromorphic applications and reducing practical system design complexity. Our device also demonstrates excellent

**Fig. 6 | Effect of channel with etched holes on ECRAM's dynamic range.** **a** Optical image of the graphene device. **b** Schematic of the lithium ions intercalating into bilayer graphene through a hole. **c** Conductance changes over time during lithium-ion intercalation in three devices. **d** Box chart shows the distribution of graphene device samples for pristine, single hole, and double hole in 3000 s.



long-term retention and endurance, as confirmed by additional measurements (Figs. S8 and S9).

Besides pulse modulation, our study emphasized the substantial influence of geometric factors on device performance. By comparing devices with varying channel lengths and etched hole designs, we found that geometric structures directly impact ion intercalation efficiency. Longer channel edges increase effective intercalation areas, thereby enhancing the dynamic range. Detailed structural analyses revealed that optimized geometric designs, such as etched holes, accelerate ion intercalation, offering targeted engineering strategies to further boost device performance. Detailed structural analyses revealed that optimized geometric designs—particularly the introduction of etched holes into the bilayer graphene channels—can significantly accelerate lithium-ion intercalation. The engineered holes increase the number of accessible edge sites, which first-principles calculations identify as more favorable for Li insertion than vacancy-assisted pathways, suggesting that edge sites likely serve as the dominant intercalation channels. By shortening the effective diffusion length and enhancing ion accessibility, such geometries offer a practical and scalable strategy for improving both the speed and efficiency of device response. These findings provide a clear direction for future device optimization through targeted structural engineering.

In addition to these results, we observed performance variations across devices, as shown in the box plots in Figs. 3 and 6. Such variability is common in systems using mechanically exfoliated 2D materials. Differences in flake geometry, layer thickness, edge quality, and local material uniformity can significantly affect ion intercalation behavior and conductance response. Misalignment between the flake and electrodes, as well as uneven ionic contact, may further contribute to the spread. Despite these variations, the overall trends remain consistent. Reducing variability is essential for future large-scale applications. Wafer-scale fabrication methods, such as chemical vapor deposition (CVD), combined with precise lithographic patterning, may improve uniformity and reproducibility. These advances will support the integration of bilayer graphene synaptic devices into scalable neuromorphic systems.

In summary, our findings advance the understanding of  $\text{Li}^+$  intercalation dynamics in bilayer graphene and offer valuable insights for designing high-performance artificial synapses in neuromorphic computing. By systematically examining pulse parameters and geometric structures from multiple perspectives, we identified key mechanisms governing ion behavior, providing theoretical and experimental

foundations for future investigations into long-term cycling stability, scalability, and multi-layer integration. This systematic approach to electrochemical and structural parameters establishes a robust basis for developing tunable artificial synapses. Energy-efficient and high-performance neuromorphic computing systems require devices that not only feature suitable dynamic ranges but also sustain stability and responsiveness over extended periods. Our results demonstrate that optimizing driving conditions and physical structures significantly enhances device energy efficiency and operational flexibility while maintaining excellent performance. Not all neuromorphic or memory applications require the full dynamic range of a synaptic device. In many cases, a limited range suffices for effective computation or storage. Pulse modulation offers a direct means to access the desired conductance state without completing full intercalation cycles. By reducing duty cycle or amplitude, lithium-ion migration can be curtailed, leading to significant energy savings. This targeted control enables energy-efficient operation without compromising functionality. Rather than defaulting to maximum dynamic range—which often causes unnecessary ion displacement and increased power usage—our approach supports task-specific tuning. This strategy not only reduces energy consumption but also minimizes material fatigue and prolongs device lifespan. It presents a practical pathway towards scalable, low-power neuromorphic systems.

## Methods

### Computational methods

All first-principles calculations were performed using the projector augmented wave (PAW) method<sup>67</sup>, as implemented in the Vienna Ab initio Simulation Package (VASP)<sup>68–70</sup>. The exchange-correlation energy was treated using the generalized gradient approximation (GGA) with the Perdew–Burke–Ernzerhof (PBE) functional<sup>71</sup>. Van der Waals interactions were accounted for using DFT-D3 dispersion correction<sup>72</sup>. Spin polarization was included in all calculations to accurately describe systems containing unpaired electrons.

The plane-wave kinetic energy cutoff was set to 400 eV. Electronic convergence was achieved when the total energy change between successive electronic steps was less than  $10^{-4}$  eV. Structural relaxations were performed using the conjugate gradient (CG) algorithm, with all atomic positions relaxed until the residual forces were below 0.01 eV/Å.

A vacuum spacing of at least 15 Å was applied along the non-periodic direction in all calculations to prevent interactions between periodic images.

For nanoribbon models used to simulate edge insertion, all exposed edge carbon atoms were passivated with hydrogen.

The Brillouin zone was sampled using  $\Gamma$ -centered grids. For small  $3 \times 3$  bilayer graphene supercells, an  $8 \times 8 \times 1$  k-point mesh was employed. For larger  $6 \times 6$  supercells, a  $4 \times 4 \times 1$  mesh was employed. In nanoribbon systems with periodicity along one dimension, the Brillouin zone was sampled with an 8-point  $\Gamma$ -centered k-grid along the periodic direction, and  $\Gamma$ -point sampling in the non-periodic directions.

To investigate lithium (Li) insertion pathways and diffusion barriers, we employed the climbing-image nudged elastic band (CI-NEB) method<sup>73</sup>. For vacancy-mediated insertion paths, the NEB included 5 intermediate images interpolating between the initial and final states. For edge-insertion studies using nanoribbons, 14 intermediate images were used. All NEB calculations were relaxed until the maximum force on any atom in all images was below 0.05 eV/Å.

All calculations are performed for a neutral system, though the net charge on the Li atom can be non-zero depending on the distance to carbon atoms as a result of charge transfer between the graphene and Li.

## Device fabrication

Bilayer graphene flakes were obtained through mechanical exfoliation and transferred onto a SiO<sub>2</sub> (90 nm) layer on a Si substrate. 950 PMMA A4 resist was spin-coated onto the sample. The electrode patterns were defined using electron beam lithography (EBPG), and an e-beam evaporator to deposit 80 nm Au with a 1.5 nm Ti adhesion layer onto the graphene surface. Two ionic gates were then deposited near the graphene device: one using 80 nm Au with a 1.5 nm Ti, and the other using 80 nm Pt with a 1.5 nm Ti. LiFePO<sub>4</sub> (LFP) solution was dropped onto the ionic gates and baked at 80 °C for 30 min. The electrolyte solution was prepared in a glovebox with 15 ml of Acetonitrile, 0.3 g of LiClO<sub>4</sub>, and 1 g of PEO, stirred overnight at 50 °C. LiClO<sub>4</sub>/PEO solution was dropped onto the graphene device and ionic gates. The device was baked at 80°C for 24 h. The device was transferred to the vacuum probe station for measurements.

## Raman spectroscopy and AFM characterization

Raman spectroscopy was performed using a Horiba LabRam instrument with a 473 nm laser. The measurements were conducted using a 100x objective, resulting in a laser spot radius of approximately 300 nm. Atomic Force Microscopy (AFM) characterization was conducted using a Bruker instrument in tapping mode over a 10 μm range to further confirm the bilayer graphene structure and surface morphology.

## Electrical and electrochemical characterization

All electrochemical characterizations were performed with Keithley Semiconductor Parameter Analyzer (4200-SCS) with pulse measuring units. During galvanostatic charge/discharge measurements, the graphene device was connected to the working electrode, while the LFP acted as the counter/reference electrode by applied small current. All electrical and pulse measurements were performed in a vacuum probe station to ensure accuracy and prevent environmental interference.

## Pulse modulation experiments

Pulse modulation experiments were performed with the AFG3252C arbitrary/function generator, operating in burst mode. The generated pulses were first verified for accuracy using an MDO3034 mixed-domain oscilloscope before being connected to the vacuum probe station for further measurements. This ensured the precision and reliability of the pulse signals applied during the experiments.

## Hole etching on graphene

Geometric modifications were carried out by patterning holes on the graphene surface using EBPG. The patterned graphene was then subjected to O<sub>2</sub> etching using a Plasma Asher (March PX-500) to complete the process<sup>74</sup>.

## Declaration of generative AI and AI-assisted technologies in the writing process

OpenAI ChatGPT model was utilized for proofreading and correcting typos and grammatical errors.

## Data availability

The data supporting this study are included in the main text, the supplementary Information and the simulation results. Additional datasets can be obtained from the corresponding authors upon reasonable request. All computational data is available at <https://github.com/Simon-Cao-Git/npjuc-bilayer-graphene-synapse/>.

Received: 6 June 2025; Accepted: 2 September 2025;

Published online: 01 December 2025

## References

- Dai, S. et al. Recent advances in transistor-based artificial synapses. *Adv. Funct. Mater.* **29**, 1903700 (2019).
- Pedretti, G. et al. Memristive neural network for on-line learning and tracking with brain-inspired spike timing dependent plasticity. *Sci. Rep.* **7**, 5288 (2017).
- Zidan, M. A., Strachan, J. P. & Lu, W. D. The future of electronics based on memristive systems. *Nat. Electron.* **1**, 22–29 (2018).
- Yang, C. et al. All-solid-state synaptic transistor with ultralow conductance for neuromorphic computing. *Adv. Funct. Mater.* **28**, 1804170 (2018).
- Yao, B. et al. Non-volatile electrolyte-gated transistors based on graphdiyne/MoS<sub>2</sub> with robust stability for low-power neuromorphic computing and logic-in-memory. *Adv. Funct. Mater.* **31**, 2100069 (2021).
- Yu, H. et al. Evolution of bio-inspired artificial synapses: materials, structures, and mechanisms. *Small* **17**, 2000041 (2021).
- Zhang, Z.-C., Chen, X.-D. & Lu, T.-B. Recent progress in neuromorphic and memory devices based on graphdiyne. *Sci. Technol. Adv. Mater.* **24**, 2196240 (2023).
- Kireev, D. et al. Metaplastic and energy-efficient biocompatible graphene artificial synaptic transistors for enhanced accuracy neuromorphic computing. *Nat. Commun.* **13**, 4386 (2022).
- Kwak, H., Kim, N., Jeon, S., Kim, S. & Woo, J. Electrochemical random-access memory: recent advances in materials, devices, and systems towards neuromorphic computing. *Nano Convergence* **11**, 9 (2024).
- Kuzum, D., Yu, S. & Philip Wong, H.-S. Synaptic electronics: materials, devices and applications. *Nanotechnology* **24**, 382001 (2013).
- Li, Y. et al. Low-voltage, CMOS-free synaptic memory based on Li<sub>x</sub> TiO<sub>2</sub> redox transistors. *ACS Appl. Mater. Interfaces* **11**, 38982–38992 (2019).
- Jang, N., Kwon, Y. H., Seong, N.-J., Choi, K. & Yoon, S.-M. Synergistic approaches to minimize device footprint and energy consumption in vertical-channel synapse transistors using an InGaZnO active layer via spacer engineering of HfO<sub>2</sub>. *ACS Appl. Mater. Interfaces* **17**, 40788–40797 (2025).
- Cao, Y. et al. Advanced artificial synaptic thin-film transistor based on doped potassium ions for neuromorphic computing via third-generation neural network. *J. Mater. Chem. C* **10**, 3196–3206 (2022).
- Kim, S., Lim, M., Kim, Y., Kim, H.-D. & Choi, S.-J. Impact of synaptic device variations on pattern recognition accuracy in a hardware neural network. *Sci. Rep.* **8**, 2638 (2018).
- Parmar, M. M., Gangavarapu, P. R. Y. & Naik, A. K. Dynamic range tuning of graphene nanoresonators. *Appl. Phys. Lett.* **107**, 113108 (2015).
- Wei, H. et al. Mimicking efferent nerves using a graphdiyne-based artificial synapse with multiple ion diffusion dynamics. *Nat. Commun.* **12**, 1068 (2021).

17. Tang, J. et al. ECRAM as scalable synaptic cell for high-speed, low-power neuromorphic computing. In *2018 IEEE International Electron Devices Meeting (IEDM)*. 13.1.1–13.1.4 (IEEE, San Francisco, CA, 2018).
18. Liang, C., Wang, F. & Tang, S. Two-dimensional ordering governs the overpotential of Li intercalation and plating on graphene and its variants. *J. Appl. Phys.* **131**, 165001 (2022).
19. Manthiram, A. A reflection on lithium-ion battery cathode chemistry. *Nat. Commun.* **11**, 1550 (2020).
20. Nikam, R. D. et al. Near ideal synaptic functionalities in Li ion synaptic transistor using Li<sub>3</sub>POxSex electrolyte with high ionic conductivity. *Sci. Rep.* **9**, 18883 (2019).
21. Fuller, E. J. et al. Li-ion synaptic transistor for low power analog computing. *Adv. Mater.* **29**, 1604310 (2017).
22. Haile, S. M. Fuel cell materials and components★☆☆The Golden Jubilee Issue—selected topics in materials science and engineering: past, present and future, edited by S. Suresh. *Acta Materialia* **51**, 5981–6000 (2003).
23. Talin, A. A., Li, Y., Robinson, D. A., Fuller, E. J. & Kumar, S. ECRAM materials, devices, circuits and architectures: a perspective. *Adv. Mater.* **35**, 2204771 (2023).
24. Mukhtar, M., Sultan, M. J., Ali, U. & Lee, S. Y. Trends in hydrogen, lithium and oxygen-based electrochemical RAM: materials, mechanisms, and applications. *J. Mater. Chem. C* **13**, 17458–17482 (2025).
25. Yu, C. et al. Gate-controlled neuromorphic functional transition in an electrochemical graphene transistor. *Nano Lett.* **24**, 1620–1628 (2024).
26. He, X. et al. Long-ionic-gated graphene synaptic transistor with enhanced memory, learning function and humidity perception. *Appl. Phys. Lett.* **124**, 053501 (2024).
27. Zhou, J. et al. First-principles study of lithium intercalated bilayer graphene. *Sci. China Phys. Mech. Astron.* **55**, 1376–1382 (2012).
28. Zou, J., Sole, C., Drewett, N. E., Velický, M. & Hardwick, L. J. In situ study of li intercalation into highly crystalline graphitic flakes of varying thicknesses. *J. Phys. Chem. Lett.* **7**, 4291–4296 (2016).
29. Bi, J. et al. On the road to the frontiers of lithium-ion batteries: a review and outlook of graphene anodes. *Adv. Mater.* **35**, 2210734 (2023).
30. Cai, Z. et al. Dynamic study of intercalation/deintercalation of ionic liquids in multilayer graphene using an alternating current Raman spectroscopy technique. *J. Phys. Chem. Lett.* **14**, 7223–7228 (2023).
31. Joy, R. et al. Graphene: Chemistry and applications for lithium-ion batteries. *Electrochem* **3**, 143–183 (2022).
32. Kucinskis, G., Bajars, G. & Kleperis, J. Graphene in lithium ion battery cathode materials: a review. *J. Power Sources* **240**, 66–79 (2013).
33. Li, N., Chen, Z., Ren, W., Li, F. & Cheng, H.-M. Flexible graphene-based lithium ion batteries with ultrafast charge and discharge rates. *Proc. Natl. Acad. Sci. USA* **109**, 17360–17365 (2012).
34. Liang, M. & Zhi, L. Graphene-based electrode materials for rechargeable lithium batteries. *J. Mater. Chem.* **19**, 5871 (2009).
35. Moulsdale, C., Enaldiev, V. V., Geim, A. K. & Fal'ko, V. I. Non-chiral one-dimensional states inside AB/BA domain walls in bilayer graphene. *Acad. Nano Sci. Mater. Technol.* **1**, <https://doi.org/10.20935/AcadNano7267> (2024).
36. Raccichini, R., Varzi, A., Wei, D. & Passerini, S. Critical insight into the relentless progression toward graphene and graphene-containing materials for lithium-ion battery anodes. *Adv. Mater.* **29**, 1603421 (2017).
37. Sehrawat, P., Shabir, A., Abid, Julien, C. M. & Islam, S. S. Recent trends in silicon/graphene nanocomposite anodes for lithium-ion batteries. *J. Power Sources* **501**, 229709 (2021).
38. Sui, D. et al. A comprehensive review of graphene-based anode materials for lithium-ion capacitors. *Chemistry* **3**, 1215–1246 (2021).
39. Thomas, S., Nam, E. B. & Lee, S. U. Atomistic dynamics investigation of the thermomechanical properties and Li diffusion kinetics in  $\psi$ -graphene for LIB anode material. *ACS Appl. Mater. Interfaces* **10**, 36240–36248 (2018).
40. Ji, K. et al. Lithium intercalation into bilayer graphene. *Nat. Commun.* **10**, 275 (2019).
41. Astles, T. et al. In-plane staging in lithium-ion intercalation of bilayer graphene. *Nat. Commun.* **15**, 6933 (2024).
42. Kühne, M. et al. Ultrafast lithium diffusion in bilayer graphene. *Nat. Nanotech* **12**, 895–900 (2017).
43. Nikam, R. D., Kwak, M., Lee, J., Rajput, K. G. & Hwang, H. Controlled ionic tunneling in lithium nanoionic synaptic transistor through atomically thin graphene layer for neuromorphic computing. *Adv. Electr. Mater.* **6**, 1901100 (2020).
44. Rajapakse, M. et al. Intercalation as a versatile tool for fabrication, property tuning, and phase transitions in 2D materials. *npj 2D Mater. Appl.* **5**, 30 (2021).
45. Li, H.-M. et al. Electric double layer dynamics in poly(ethylene oxide) LiClO<sub>4</sub> on graphene transistors. *J. Phys. Chem. C* **121**, 16996–17004 (2017).
46. Tao, R. et al. Kinetics tuning the electrochemistry of lithium dendrites formation in lithium batteries through electrolytes. *ACS Appl. Mater. Interfaces* **9**, 7003–7008 (2017).
47. Hao, Y. et al. Probing layer number and stacking order of few-layer graphene by Raman spectroscopy. *Small* **6**, 195–200 (2010).
48. Shen, Z., Li, J., Yi, M., Zhang, X. & Ma, S. Preparation of graphene by jet cavitation. *Nanotechnology* **22**, 365306 (2011).
49. Cai, X., Lai, L., Shen, Z. & Lin, J. Graphene and graphene-based composites as Li-ion battery electrode materials and their application in full cells. *J. Mater. Chem. A* **5**, 15423–15446 (2017).
50. Sharbati, M. T. et al. Low-power, electrochemically tunable graphene synapses for neuromorphic computing. *Adv. Mater.* **30**, 1802353 (2018).
51. Bao, W. et al. approaching the limits of transparency and conductivity in graphitic materials through lithium intercalation. *Nat. Commun.* **5**, 4224 (2014).
52. Guo, Y. et al. Li Intercalation into graphite: direct optical imaging and Cahn–Hilliard reaction dynamics. *J. Phys. Chem. Lett.* **7**, 2151–2156 (2016).
53. Rykner, M. & Chandesris, M. Free energy model for lithium intercalation in graphite: focusing on the coupling with graphene stacking sequence. *J. Phys. Chem. C* **126**, 5457–5472 (2022).
54. Yi, S., Wang, B., Chen, Z., Wang, R. & Wang, D. A study on LiFePO<sub>4</sub>/graphite cells with built-in Li<sub>4</sub>Ti<sub>5</sub>O<sub>12</sub> reference electrodes. *RSC Adv.* **8**, 18597–18603 (2018).
55. Zhong, K. et al. Adsorption and ultrafast diffusion of lithium in bilayer graphene: ab initio and kinetic Monte Carlo simulation study. *Phys. Rev. B* **99**, 155403 (2019).
56. Nashashibi, S. et al. Engineering graphene phototransistors for high dynamic range applications. *ACS Nano* **18**, 12760–12770 (2024).
57. Pradhan, N. R. et al. Photoconductivity of few-layered p-WSe<sub>2</sub> phototransistors via multi-terminal measurements. *2D Mater.* **3**, 041004 (2016).
58. Geng, C.-Y., Yu, J. & Shi, F.-N. Electrochemical study on different layers of graphene based TiO<sub>2</sub>/graphene composites as an anode for lithium-ion batteries. *Res. Chem. Intermed.* **45**, 3409–3424 (2019).
59. Shu, H., Chen, X. & Ding, F. The edge termination controlled kinetics in graphene chemical vapor deposition growth. *Chem. Sci.* **5**, 4639–4645 (2014).
60. Zhang, X. et al. Experimentally engineering the edge termination of graphene nanoribbons. *ACS Nano* **7**, 198–202 (2013).
61. Endo, Y. et al. Dynamic topological domain walls driven by lithium intercalation in graphene. *Nat. Nanotechnol.* **18**, 1154–1161 (2023).
62. Dong, Y. et al. Challenges and strategies of fast-charging Li-ion batteries with a focus on Li plating. *Energy Mater. Adv.* **5**, 0113 (2024).
63. Lee, H. et al. Vertical metal-oxide electrochemical memory for high-density synaptic array based high-performance neuromorphic computing. *Adv. Electr. Mater.* **8**, 2200378 (2022).

64. Nikam, R. D., Kwak, M. & Hwang, H. All-solid-state oxygen ion electrochemical random-access memory for neuromorphic computing. *Adv. Electr. Mater.* **7**, 2100142 (2021).
65. Oh, S. et al. HfZrO<sub>x</sub>-Based ferroelectric synapse device with 32 levels of conductance states for neuromorphic applications. *IEEE Electron Device Lett.* **38**, 732–735 (2017).
66. Krishnaprasad, A. et al. Graphene/MoS<sub>2</sub>/SiO<sub>x</sub> memristive synapses for linear weight update. *npj 2D Mater. Appl.* **7**, 22 (2023).
67. Blöchl, P. E. Projector augmented-wave method. *Phys. Rev. B* **50**, 17953–17979 (1994).
68. Kresse, G. & Hafner, J. Ab initio molecular dynamics for liquid metals. *Phys. Rev. B* **47**, 558–561 (1993).
69. Kresse, G. & Furthmüller, J. Efficiency of ab-initio total energy calculations for metals and semiconductors using a plane-wave basis set. *Comput. Mater. Sci.* **6**, 15–50 (1996).
70. Kresse, G. & Furthmüller, J. Efficient iterative schemes for ab initio total-energy calculations using a plane-wave basis set. *Phys. Rev. B* **54**, 11169–11186 (1996).
71. Perdew, J. P., Burke, K. & Ernzerhof, M. Generalized gradient approximation made simple. *Phys. Rev. Lett.* **77**, 3865–3868 (1996).
72. Grimme, S., Antony, J., Ehrlich, S. & Krieg, H. A consistent and accurate ab initio parametrization of density functional dispersion correction (DFT-D) for the 94 elements H–Pu. *J. Chem. Phys.* **132**, 154104 (2010).
73. Henkelman, G., Uberuaga, B. P. & Jónsson, H. A climbing image nudged elastic band method for finding saddle points and minimum energy paths. *J. Chem. Phys.* **113**, 9901–9904 (2000).
74. Bobadilla, A. D., Ocola, L. E., Sumant, A. V., Kaminski, M. & Seminario, J. M. PMMA-assisted plasma patterning of graphene. *J. Nanotechnol.* **2018**, 1–8 (2018).

## Acknowledgements

Y.H., Y.L., and F.X. acknowledge support from the U.S. National Science Foundation (NSF) under Grants ECCS-1943683, 1955453. P.C., S.H., K.J., R.K., M.P.A., and F.X. were partly supported by the NSF Future of Semiconductors (FuSe) award 2328815 and NSF Future of Manufacturing Seed Grant 2229131. D.V. and N.Y. were supported by the NSF award 2227459. Work performed in the University of Pittsburgh Dietrich School Materials Characterization Laboratory (RRID:SCR\_025127) and services and instruments used in this project were graciously supported, in part, by the University of Pittsburgh.

## Author contributions

Y.H.: conceptualization, methodology, performing experiments, preparing the figures and writing—original draft, writing—review & editing. P.C.: performed and analyzed all DFT simulations, including interlayer diffusion and insertion pathways, and contributed to the interpretation of

computational results in relation to experimental findings. S.H.: contributing to draft development, reviewing the manuscript, and assisting with figure preparation. Y.L.: providing suggestions on conceptualization and assisting with proof-checking the draft. D.V.: performing the AFM measurement. K.J.: contributed to early-stage calculations of lithium insertion through a 1C vacancy and participated in related discussions. N.Y. and R.K.: providing suggestions during draft preparation, reviewing, and proof-checking the draft. M.P.A. and F.X.: conceptualization, funding acquisition, methodology, project administration, supervision, validation, writing—review & editing. All authors reviewed and discussed the results. Y.H. and P.C.: wrote the draft manuscript. All authors contributed to the completion of the manuscript.

## Competing interests

The authors declare no competing interests.

## Additional information

**Supplementary information** The online version contains supplementary material available at <https://doi.org/10.1038/s44335-025-00042-4>.

**Correspondence** and requests for materials should be addressed to Feng Xiong.

**Reprints and permissions information** is available at <http://www.nature.com/reprints>

**Publisher's note** Springer Nature remains neutral with regard to jurisdictional claims in published maps and institutional affiliations.

**Open Access** This article is licensed under a Creative Commons Attribution-NonCommercial-NoDerivatives 4.0 International License, which permits any non-commercial use, sharing, distribution and reproduction in any medium or format, as long as you give appropriate credit to the original author(s) and the source, provide a link to the Creative Commons licence, and indicate if you modified the licensed material. You do not have permission under this licence to share adapted material derived from this article or parts of it. The images or other third party material in this article are included in the article's Creative Commons licence, unless indicated otherwise in a credit line to the material. If material is not included in the article's Creative Commons licence and your intended use is not permitted by statutory regulation or exceeds the permitted use, you will need to obtain permission directly from the copyright holder. To view a copy of this licence, visit <http://creativecommons.org/licenses/by-nc-nd/4.0/>.

© The Author(s) 2025